Peak-*SNR* Analysis of CMOS TDCs for SPAD-Based TCSPC 3D Imaging Applications

Foad Arvani and Anthony Chan Carusone, *Senior Member, IEEE*

Abstract—TDCs formed by ring oscillators are arrayable, scalable, and low power, making them suitable for SPAD-based TCSPC 3D imaging systems. The TDC precision affects the ranging accuracy and, hence, the quality of the reconstructed 3D image. This brief studies the jitter of ring-oscillator-based TDCs as a function of their full-scale-range and derives an expression for the TDC total jitter. The introduced behavioral model describes three different regions of the *SNR* for TDCs. A peak-*SNR* design-point is identified. Increasing the full-scale-range of the TDC beyond this point entails increased jitter and, thus, ultimately a declining *SNR*. The analysis is validated using post-layout simulations of a ring-oscillator-based TDC designed in 65nm CMOS. A TDC resolution degradation factor defines the TDC jitter behavioral model. It is consistent with FOMs that have been used in the past to evaluate TDCs and clarifies their underlying assumptions.

Index Terms—Time-correlated single-photon counting (TCSPC), LiDAR, single-photon avalanche diode (SPAD), time-to-digital converter (TDC), time-of-flight (TOF), ring oscillator, frequency divider, jitter, SNR, CMOS, figure-of-merit.

I. INTRODUCTION

RECENTLY, industry and academia have shown a high interest in three-dimensional (3D) imaging sensors and systems, with emerging applications in entertainment, engineering, and science being the primary drivers of market growth in this area [1]–[3]. Among the solutions presented in the literature, implementations based on the single-photon avalanche diode (SPAD) CMOS time-of-flight (TOF) method have proven to be compact, low cost, and highly integrated fulfilling the needs of battery-powered devices [1], [2]. SPADs can detect the arrival time of individual photons in light detection and ranging (LiDAR) systems with jitter as low as few tens of picoseconds [4]. Thus, they offer the precision and accuracy required for sub-millimeter spatial resolution in time-correlated single-photon counting (TCSPC) LiDAR modules.

There are voltage-domain [5] and time-domain [6] methods for digitizing the photons' time-of-arrival. Unlike voltage- or current-domain signals, which are limited by reference or supply voltages, time-domain signals are limited by the measurement duration. Time-to-digital converters (TDCs) comprise the

core of time-domain digitizers. Thus, their jitter affects the variance of the measured distance and, hence, the quality of the reconstructed 3D image. There are trade-offs between jitter and the maximum measurable time-interval that are not captured by the figures-of-merit (FOMs) traditionally applied to TDCs in other applications [7] such as digital PLLs (DPLLs).

This brief studies the jitter of arrayble ring oscillator (RO)-based TDCs as a function of their full-scale-range. We show that TDCs intended for short, medium, and long-range TOF measurements exhibit fundamentally different *SNR* limitations. Moreover, there is a peak-*SNR* design-point. Our analysis is consistent with TDC FOMs that have been used in the past [7]–[9] revealing their underlying assumptions and unifying them for the digitization of short, medium, and long time-intervals.

First, Section II provides a brief background on SPADs, TCSPC systems, and time-of-flight digitization methods emphasizing RO-based TDCs as an arrayable and scalable TDC architecture for SPAD-based imaging systems. Section III analyzes the jitter of RO-based TDCs in terms of the time-interval being digitized, relating it to TDC FOMs introduced in the literature. We identify the peak-*SNR* design-point and highlight the suitability of RO-based TDCs for SPAD-based LiDAR systems. We validate the analysis with post-layout simulations of an RO-based TDC designed in 65nm CMOS.

II. BACKGROUND

A. SPADs and TCSPC Systems

SPADs are avalanche photodetectors (APD) biased at a voltage that exceeds the reverse breakdown voltage of the junction so that absorption of a single photon is sufficient to initiate avalanche. The high sensitivity and low jitter (a few tens of picoseconds) of SPADs [4] motivated their widespread use in both scientific and industrial applications. As shown in Fig. 1, in SPAD-based TOF TCSPC distance measurement, a modulated light source, typically a laser, repetitively illuminates the scene [2]. The reflected pulses are detected by a SPAD array [2]. The power of the light source is such that only one reflected photon (or none) is typically received by each SPAD each excitation cycle. The measurement is repeated, and the output of each pixel is a time-stamped sequence of pulses coinciding with the first photon arrivals within each repetition period T_{mod} [10]. The detected photons include false triggers generated by background light or dark counts [2]. This arrival sequence creates a histogram, the basis for calculating the time-of-flight, as shown in Fig. 2 [11]. Reflected photon time-of-flight is, in turn, related to the range of the reflecting target by the speed of light.

The precision of the measured distance is largely determined by the finite resolution and jitter of the TDC, which together give rise to a timing variance, σ_{TDC}^2.
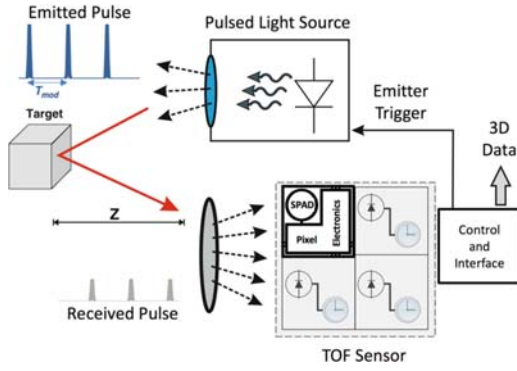
Fig. 1. A typical SPAD-based TCSPC 3D imaging system block diagram [2]; a modulated/pulsed LED/LASER typically in the infrared band illuminates the target and an array of SPAD photo-detectors (pixels) detect the received light with single-photon sensitivity. The in-pixel electronics time-stamp the photon arrival time (the time-of-flight).
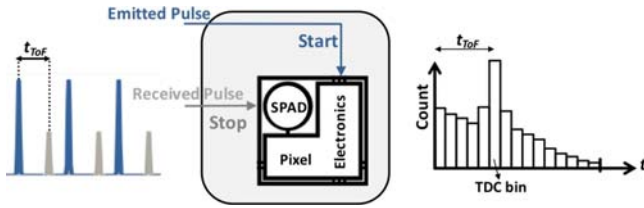

Fig. 2. A repetitive trigger from the emitter starts the counter and detected arrivals from the SPAD stop the counter; the in-pixel electronics consisting of a TDC digitize the measurement period $T_{sig} = T_{stop} - T_{start}$ resulting in the time-of-flight histogram on the right.

B. Arrayable TDC Structure for SPAD-Based LiDAR Systems

The RO-based TDC and its variants are well suited to 3D imaging applications since they can achieve a high resolution of tens of picoseconds and wide dynamic range of hundreds of nanoseconds within a small area (comparable to that of the SPADs) and power dissipation less than 1mW [10], [12], [13]. The multiple clock phases in a single RO can be shared by an array of TDCs on the same chip. In such an architecture, the frequency of the RO can be tuned to adjust the TDC resolution.

III. JITTER OF RO-BASED TDCs AND THE PEAK-SNR

Figure 3 shows one variant of the RO-based TDC. The RO drives a counter. Incoming pulses take a snapshot of the counter output and of the RO phases for fine time-resolution. The TDC output has several sources of error including the quantization error σ_q, the ring oscillator jitter σ_{RO}, and the counter jitter σ_{CN}. Thus, the time-precision is

$$\sigma_{TDC}^2 = \sigma_q^2 + \sigma_{RO}^2 + \sigma_{CN}^2. \tag{1}$$

A. The Counter Jitter: σ_{CN}

A typical counter is a cascade of frequency dividers (FD) as shown in Fig. 4, each contributing additional jitter σ_{FD} on each transition of the input clock as it propagates along the cascade of flip-flops. Assuming an input frequency of f_{Osc} from the ring oscillator and a measurement period of T_{sig}, the number of FD stages used for the measurement is $log_2\lceil T_{sig}f_{Osc}\rceil$.

Assuming identical FD stages in the counter, the jitter contributed by the asynchronous multi-stage counter will be

$$\sigma_{CN}^2 = \sigma_{FD}^2 log_2\lceil T_{sig}f_{Osc}\rceil. \tag{2}$$

Investing in a re-timer can remove the counter-induced jitter. However, based on our analysis, counter-induced jitter is only
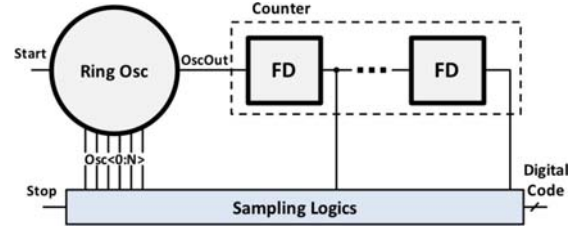

Fig. 3. An arrayble RO-based TDC structure for SPAD-based TCSPC LiDAR application consisting of a $(N + 1)$-stage ring oscillator driving a counter implemented as a cascade of frequency dividers (FD) to extend the dynamic range.
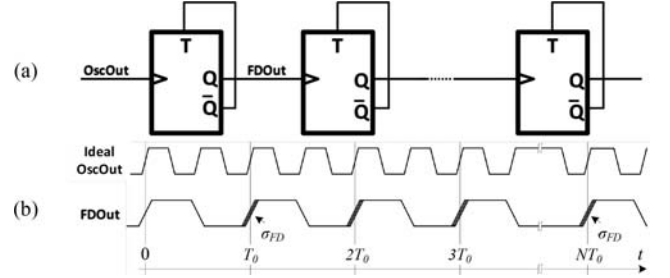

Fig. 4. (a) The counter consisting of a cascade of toggle-flip-flops as frequency dividers; (b) with an ideal input signal, the cycle and absolute jitter of a frequency divider are the same, and each stage contributes an additional absolute jitter σ_{FD}.

the bottleneck when measuring very short ranges (less than one meter), which are not of primary interest in many 3D imaging applications.

B. The Ring Oscillator Jitter: σ_{RO}

The general relationship between the jitter of a ring oscillator and its phase noise $\mathcal{L}(f)$ is [14]

$$\sigma_{RO}^2 = \int_0^\infty 2\mathcal{L}(f)\frac{sin^2(\pi f/f_{Osc})}{(\pi f_{Osc})^2}df. \tag{3}$$

It is not trivial to solve this integral analytically for flicker-induced phase noise. However, an estimate of the integrated jitter variance in radians squared is [15]

$$\sigma_{RO}^2 \cong \left(\frac{1}{2\pi f_{Osc}}\right)^2 \int_{f_1}^{f_2} 2\mathcal{L}(f)df. \tag{4}$$

Commonly the upper integration limit is determined by the oscillating frequency, $f_2 = f_{Osc}/2$. The lower integration limit is determined by how long the oscillator runs prior to the measurement, $f_1 = 1/T_{sig}$, which in turn depends on the target's range, (*speed of light*)$/2T_{sig}$. Assuming the RO is reset with each emitted pulse, $T_{sig} \le T_{mod}$ holds, as shown in Fig. 1.

Substituting (2) and (4) into (1), the total RMS value of the RO-based TDC precision depends on the measurement period T_{sig} as follows:

$$\sigma_{TDC}^2 \cong \sigma_q^2 + \frac{\int_{f_1=1/T_{Sig}}^{f_2=f_{Osc}/2} 2 \cdot \mathcal{L}(f)df}{(2\pi f_{Osc})^2} + \sigma_{FD}^2 log_2\lceil T_{sig}f_{Osc}\rceil. \tag{5}$$

C. The Ring Oscillator Jitter Versus the Target's Range

Typically, the oscillator phase noise at an offset frequency f from the carrier, $\mathcal{L}(f)$, can be treated as a wide-sense stationary random process and approximated as a sum of power-law

processes $h_i f^{-i}$ [16]

$$\mathcal{L}(f) = h_0 + \frac{h_1}{f} + \frac{h_2}{f^2} + \frac{h_3}{f^3} + \frac{h_4}{f^4}. \tag{6}$$

Corner frequencies f_c and f_a mark, respectively, the transition between $1/f^2$ and $1/f^3$, and between $1/f^3$ and $1/f^4$-dominated portions of the phase noise, as shown in Fig. 5a. Typically, the first two terms in (6), $h_0 + h_1/f$, have a negligible contribution to the TDC precision in (5) compared to the contribution of the counter-induced jitter. Thus, while substituting (6) in (5), we can neglect these two terms. By increasing the distance to the reflective target, the f^{-2}, f^{-3}, and f^{-4} terms of the RO phase noise become dominant [17]. The target's range determines $T_{sig} = 1/2(speed\ of\ light) \times range$, which in turn determines the lower integration limit f_1 and the dominant terms in $\mathcal{L}(f)$ resulting in different slopes for the jitter versus T_{sig} (Fig. 5b).

1) Short-Range ($f_c < f_1$): When the reflective target of the light pulses is in close proximity, or when the excitation frequency is higher than the oscillator's phase noise corner frequency, $1/T_{mod} > f_c$, then we are assured $f_1 = 1/T_{sig} > f_c$. In this case, the third term in (6) is dominant, and the phase noise approximates

$$\mathcal{L}(f) \approx \frac{h_2}{f^2}. \tag{7}$$

Then, the oscillator phase noise changes at 20dB/dec throughout the integration interval leading to $\sigma_{RO}^2 \propto T_{sig}$:

$$\sigma_{RO}^2 \approx \left(\frac{1}{2\pi f_{Osc}}\right)^2 \int_{f_1}^{f_2} 2\frac{h_2}{f^2} df = \left(\frac{1}{2\pi f_{Osc}}\right)^2 2 \frac{-h_2}{f}\Big|_{1/T_{sig}}^{f_{Osc}/2}$$

$$\cong \left(\frac{1}{2\pi f_{Osc}}\right)^2 2h_2 T_{sig}. \tag{8}$$

2) Medium-Range ($f_a < f_1 < f_c$): By contrast, when there is no nearby target and the excitation frequency is less than f_c, then $f_a < f_1 < f_c$, and f^{-3} is the dominant term in the oscillator phase noise $\mathcal{L}(f)$

$$\mathcal{L}(f) \approx \frac{h_3}{f^3}. \tag{9}$$

As, a result, the phase noise roll-off is 30dB/dec within the integration interval. In this case, $\sigma_{RO}^2 \propto T_{sig}^2$:

$$\sigma_{RO}^2 \approx \left(\frac{1}{2\pi f_{Osc}}\right)^2 \int_{f_1}^{f_2} 2\frac{h_3}{f^3} df = \left(\frac{1}{2\pi f_{Osc}}\right)^2 2 \frac{-h_3}{f^2}\Big|_{1/T_{sig}}^{f_{Osc}/2}$$

$$\cong \left(\frac{1}{2\pi f_{Osc}}\right)^2 2h_3 T_{sig}^2. \tag{10}$$

3) Long-Range ($f_1 < f_a$): For sufficiently large T_{sig} where $f_1 < f_a$, in the near-carrier regime, long correlated events in the oscillator phase give rise to f^{-4} components in the oscillator power spectral density [16]:

$$\mathcal{L}(f) \approx \frac{h_4}{f^4}. \tag{11}$$

Then, σ_{RO} increases super-linearly with T_{sig}, $\sigma_{RO}^2 \propto T_{sig}^3$

$$\sigma_{RO}^2 \approx \left(\frac{1}{2\pi f_{Osc}}\right)^2 \int_{f_1}^{f_2} 2\frac{h_4}{f^4} df = \left(\frac{1}{2\pi f_{Osc}}\right)^2 2 \frac{-h_4}{f^3}\Big|_{1/T_{sig}}^{f_{Osc}/2}$$

$$\cong \left(\frac{1}{2\pi f_{Osc}}\right)^2 2h_4 T_{sig}^3. \tag{12}$$

Thus, a plot of oscillator RMS jitter versus measurement period on a log-log scale has a slope varying from 0.5 to 1 and eventually 1.5, as shown in Fig. 5b.

D. The Peak-SNR

The *SNR* of the ToF measurement is the ratio of the time signal being measured to the time measurement noise,

$$SNR = \frac{T_{sig}^2}{\sigma_{TDC}^2}. \tag{13}$$

We may equate the noisy TDC output variance to that of a noiseless TDC whose quantization interval T_{LSB} is degraded by a factor $\kappa > 1$. Specifically, for a noiseless TDC, the only non-zero term in (5) is $\sigma_q = T_{LSB}/\sqrt{12}$. A noisy TDC with output jitter variance σ_{TDC}^2 can be said to have an effective time-resolution of κT_{LSB}, which is the quantization interval that would produce the same variance in a noiseless TDC. Thus, $\sigma_{TDC}^2 = (\kappa T_{LSB})^2/12 = \kappa^2 \sigma_q^2$ and $SNR = T_{sig}^2/(\kappa^2 \sigma_q^2)$.

Note that different terms in (5) are likely to dominate depending on the measurement period, T_{sig}. The quantization noise, σ_q, remains constant irrespective of T_{sig}. To analyze the behavior of the signal-dependent jitter, TDCs with negligible quantization noise are of interest. For very small T_{sig}, it is likely that the third term, representing noise in the counter, will be larger than the RO jitter in the second term, $\sigma_{CN} > \sigma_{RO}$, resulting in

$$\kappa^2 \cong \frac{\sigma_{FD}^2 log_2 \lceil T_{sig} f_{Osc} \rceil}{\sigma_q^2}. \tag{14}$$

In this case, σ_{TDC} and κ increase sub-linearly with T_{sig} so that *SNR* improves with increasing T_{sig}. If T_{sig} is increased, the integral of RO phase noise in (5) will increase so that $\sigma_{RO} > \sigma_{CN}$ and

$$\kappa^2 \cong \frac{\sigma_{RO}^2}{\sigma_q^2} \tag{15}$$

At first, for the short-range, when T_{sig} is still smaller than $1/f_c$, the RO's phase noise is dominated by the thermal noise and exhibits 20dB/dec roll-off. Since in this region, $\sigma_{RO}^2 \propto T_{sig}$, *SNR* improves linearly with increasing T_{sig}

$$SNR \propto T_{sig}. \tag{16}$$

For medium-range measurements, where T_{sig} is between $1/f_c$ and $1/f_a$, the RO's phase noise is dominated by the accumulating flicker noise jitter and exhibits 30dB/dec roll-off. In this region, $\sigma_{RO}^2 \propto T_{Sig}^2$, κ increases linearly with increasing T_{sig}, and *SNR* starts to plateau and reach the peak-*SNR* point.

For long-range measurements, where T_{sig} is larger than $1/f_a$, the correlated near-carrier f^{-4} phase noise components result in 40dB/dec phase noise roll-off. Since $\sigma_{RO}^2 \propto T_{Sig}^3$, κ increases super-linearly with increasing T_{sig}, and *SNR* starts declining.

Moreover, (5) concludes that time-domain processing does not offer infinite *SNR* by increasing T_{sig}. By expanding the measurement period, the impact of low-frequency noise sources becomes more dominant. The delay cells must be tuned to match a fixed reference. For example, a PLL loop with a replica of the RO locked to a fixed reference frequency can be used. For long enough T_{sig}, the ring oscillator jitter is dominant, and depending on the specifications of the ring oscillator (or the reference to which it is locked), the
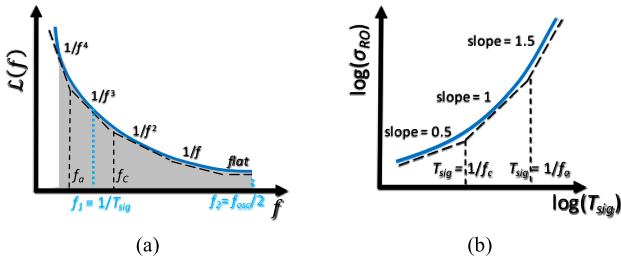
Fig. 5. (a) The oscillator phase noise at an offset frequency f from the carrier. (b) The variation of the RMS jitter with the measurement period T_{sig} for the corresponding ring oscillator.
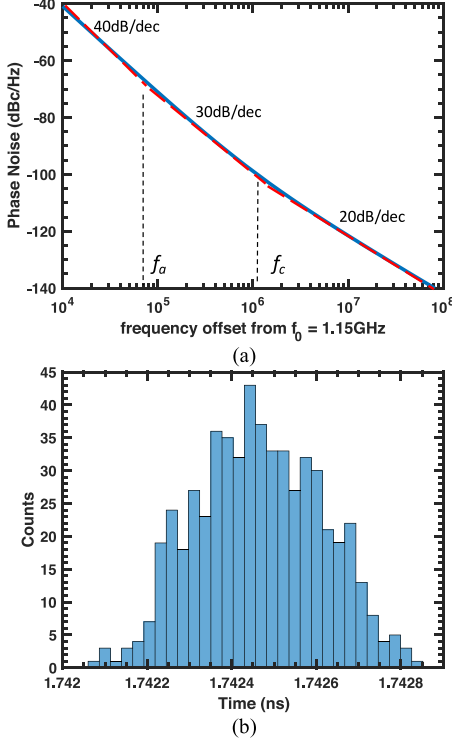

Fig. 6. (a) The post-layout PSS-simulated phase noise of the 31-stage ring oscillator with $f_a = 70$kHz and $f_c = 1$MHz. (b) The transient-noise-simulated RMS jitter of the TFF-based frequency divider stage is around 147.5fs at an input frequency of 1.15GHz.

maximum achievable *SNR* happens at a measurement period around $1/f_a$, and reduces thereafter because of the contribution of low-frequency noise sources.

E. Relationship to Previously-Published TDC FOMs

There are several FOMs in the literature to capture TDC design trade-offs. They are generally inspired by those applied to analog to digital converters (ADC) and consider DPLLs a primary application of TDCs. For a sampling rate of *BW* and power consumption of *P*, [9] suggests using

$$FOM_{1,Q} = 10log_{10}\left(\frac{P\sigma}{BW \cdot T_{sig}}\right) = 10log_{10}\left(\frac{P}{BW \cdot SNR^{0.5}}\right) \quad (17)$$

for the quantization-noise-limited case, and

$$FOM_{1,Th} = 10log_{10}\left(\frac{P\sigma^2}{BW \cdot T_{sig}}\right) = 10log_{10}\left(\frac{P\sigma}{BW \cdot SNR^{0.5}}\right) \quad (18)$$

for thermal-noise-limited operation. The former case assumes that jitter is proportional to the signal while the latter case

presumes that the jitter squared is proportional to the signal. These FOMs have different dimensionality making it complicated to compare different designs. The introduced TDC resolution degradation factor κ captures the variation of the TDC jitter versus T_{sig}. Both FOMs in [9] can be expressed in terms of κ resulting in one expression for both cases. In quantization-noise- or flicker-noise-limited operation, $\kappa \propto T_{sig}$, and in the thermal-noise-limited region, $\kappa^2 \propto T_{sig}$,

$$10log_{10}\left(\frac{P}{BW \cdot SNR^{0.5}}\right) = 10log_{10}\left(\frac{P\kappa\sigma_q}{BW \cdot T_{sig}}\right). \quad (19)$$

Similarly, [7] defines a FOM inspired by the classical ADC FOM [18]. The definition of the TDC dynamic range (DR) is not as straight forward as for ADCs. By defining the effective number of bits (*ENOB*) as the ratio of the maximum time measurement interval T_{sig} to the noise standard deviation σ, $ENOB = log_2(T_{sig}/\sigma)$, [7] suggests

$$FOM_2 = \frac{P}{BW \cdot 2^{ENOB}} = \frac{P\sigma}{BW \cdot T_{sig}} = \frac{P}{BW \cdot SNR^{0.5}} \quad (20)$$

Expressed in terms of κ, (20) is consistent with (19).

Assuming an inverter output capacitance of C_L, the total jitter of an inverter with power supply V_{DD} and propagation delay t_d due to uncorrelated white noise sources is [14]

$$\sigma^2 = t_d^2\left(\frac{8\gamma kT}{C_L V_{DD}(V_{DD} - V_{th})} + \frac{8kT}{C_L V_{DD}^2}\right). \quad (21)$$

Correspondingly, to derive a thermal noise limit for time-domain signal processing in CMOS technologies, [8] defines the *SNR* as the ratio of the inverter delay to its jitter $SNR = t_d^2/\sigma^2$. Then, assuming that jitter is proportional to the signal $\sigma^2 \propto t_d^2$, [8] uses the following FOM to compare the suitability of different technology nodes to time-domain signal processing

$$FOM_3 = \left(\frac{P}{BW \cdot SNR}\right)^{-1} = \left(\frac{P\kappa^2\sigma_q^2}{BW \cdot t_d^2}\right)^{-1}. \quad (22)$$

This FOM is also consistent with (19), assuming $T_{sig} = t_d$ and including the factor κ to generalize it for flicker noise [19].

IV. AN RO-BASED TDC FOR TCSPC 3D IMAGING

An RO-based TDC is designed in a 65nm CMOS technology for TCSPC 3D imaging applications as shown in Fig. 3 and 4. The post-layout phase noise simulation result of the 31-stage RO constructed from CMOS inverters with an oscillation frequency of 1.15GHz and loaded with a counter is shown in Fig. 6(a). Next, a transient noise simulation is performed with an ideal 1.15GHz clock applied to the toggle-flip-flop (TFF)-based frequency divider that follows the RO. Figure 6(b) is a histogram of the resulting TFF output period, revealing an RMS jitter of approximately 150fs.

The total TDC RMS jitter in Fig.7 shows that in the short-range, for a small T_{sig}, it is likely that the third term in (5), representing the counter-induced noise, will be larger than the RO jitter in the second term, $\sigma_{CN} > \sigma_{RO}$. By increasing the distance to the target, but where still $T_{sig} < 1/f_c$ holds, the RO jitter dominates, overall jitter increases sub-linearly with increasing T_{sig}, and *SNR* improves. For the medium-range, $1/f_c < T_{sig} < 1/f_a$, the RO-induced jitter increases almost linearly with increasing T_{sig}. The factor κ increases super-linearly with increasing T_{sig} after $T_{sig} = 4700$ ns and the overall RMS jitter indicates that there is a peak-*SNR* point.
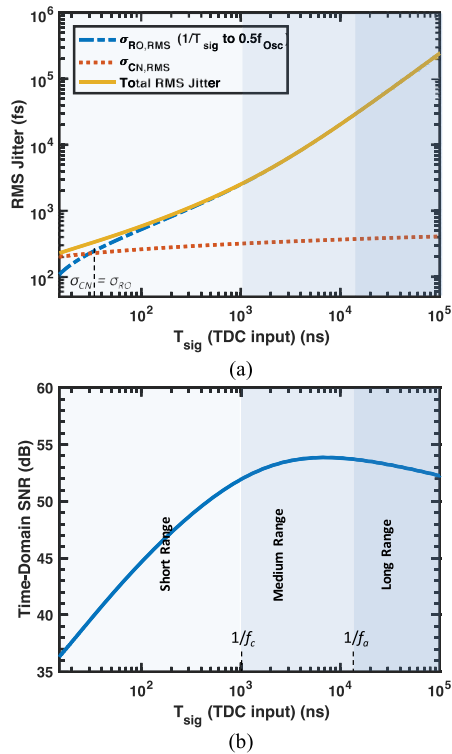
Fig. 7. (a) The post-layout simulated RMS signal-dependent jitter of the RO-based TDC versus the input measurement period T_{sig}. (b) Based on the analysis of Section III, the time-domain peak $SNR = 20log(T_{sig}/\sigma_{TDC})$ happens at a measurement period around $1/f_a$, then reduces because of the contribution of low-frequency noise sources.

In the long-range, correlated near-carrier noise sources cause a declining *SNR*.

For an indoor TCSPC LiDAR system with a range of 6m and precision of 5 mm, the time-of-flight would be around 40ns which is equivalent to an excitation frequency of 50MHz, and the required RMS precision is around 30ps. Since 50MHz is more than one decade higher than the f_c of this ring oscillator (Fig. 7) the RMS jitter of the TDC will be less than 1ps for $T_{sig} = 40$ns, which means that the RO- and counter-induced noise will not be the limiting element of the distance measurement precision for this application. Therefore, an RO-based TDC using this ring oscillator and counter would be suitable for the aforementioned indoor TCSPC LiDAR specification. Also, Fig. 7 confirms that the maximum achievable *SNR* happens at a T_{sig} around $1/f_a$ and the *SNR* declines thereafter due to low-frequency noise sources.

V. CONCLUSION

This brief derives an equation for the jitter of RO-based TDCs to assess distance measurement precision and examines their suitability for TCSPC LiDAR applications. The RMS jitter of an oscillator increases considerably with the measurement period T_{sig}. Depending on the distance to the reflective target, the oscillator exhibits different phase noise roll-offs leading to different slopes of the RMS jitter versus T_{sig}.

The introduced behavioral model describes three different regions of the *SNR* for RO-based TDCs. For the short-range, where $T_{sig} > f_c$, counter-induced jitter and thermal noise of the ring oscillator (f^{-2} component of $\mathscr{L}$) dominate the overall jitter. The signal-dependent jitter increases sub-linearly with T_{sig}, and the *SNR* improves almost linearly with increasing T_{sig}. For the medium-range, where $f_a > T_{sig} > f_c$, accumulating

flicker noise of the ring oscillator (f^{-3} component of $\mathscr{L}$) dominates the signal-dependent jitter of the TDC. In this region, the *SNR* plateaus and reaches its peak. For the long-range, the correlated near-carrier f^{-4} phase noise components start to contribute. In this region, the signal-dependent jitter increases super-linearly with increasing T_{sig}, and the *SNR* starts declining. A TDC resolution degradation factor represents the signal-dependent behavior of the jitter. The derived relationship predicts the peak-*SNR* design-point and shows that expanding the full-scale-range beyond this point does not result in infinite *SNR*. It also unifies and reveals the underlying assumptions of the TDC FOMs used in the past to evaluate TDCs, primarily for DPLLs. The derived relationship is employed to assess the jitter performance of a RO-based TDC in 65nm CMOS technology for an indoor LiDAR application.

REFERENCES

[1] P. Cambou and G. Girardin, *3D Imaging and Sensing: From Technologies to Market*, Yole Développement, Lyon, France, 2018.
[2] F. Remondino and D. Stoppa, *TOF Range-Imaging Cameras*. Heidelberg, Germany: Springer, 2013, pp. 1–240.
[3] A. Süss, *High Performance CMOS Range Imaging: Device Technology and Systems Considerations*. Boca Raton, FL, USA: CRC Press, 2016.
[4] M. J. D. Darek and P. Palubiak, "CMOS SPADs: Design issues and research challenges for detectors, circuits, and arrays," *IEEE J. Solid-State Circuits*, vol. 20, no. 6, pp. 409–426, Nov./Dec. 2014.
[5] M. Tanveer, I. Nissinen, J. Nissinen, J. Kostamovaara, J. Borg, and J. Johansson, "Time-to-digital converter based on analog time expansion for 3D time-of-flight cameras," in *Proc. Image Sens. Imag. Syst.* vol. 9022, 2014, Art. no. 90220A.
[6] Z. Cheng, M. J. Deen, and H. Peng, "A low-power gateable vernier ring oscillator time-to-digital converter for biomedical imaging applications," *IEEE Trans. Biomed. Circuits Syst.*, vol. 10, no. 2, pp. 445–454, Apr. 2016.
[7] S. Henzler, *Time-to-Digital Converters*. Dordrecht, The Netherlands: Springer 2010.
[8] A. Pathan and A. Liscidini, "Thermal noise limit for time-domain analogue signal processing in CMOS technologies," *Electron. Lett.*, vol. 52, no. 18, pp. 1567–1569, Sep. 2016.
[9] M. Straayer, "Fundamentals of time-based circuits," in *Proc. IEEE Int. Solid-State. Circuits Conf. Tuts.*, vol. T5, 2017, pp. 44–47.
[10] F. Arvani and T. C. Carusone, "TDC sharing in SPAD-based direct time-of-flight 3D imaging applications," in *Proc. IEEE Int. Symp. Circuits Syst. (ISCAS)*, Sapporo, Japan, 2019, pp. 1–5.
[11] F. Arvani and T. C. Carusone, "Direct time-of-flight TCSPC analytical modeling including dead-time effects," in *Proc. IEEE Int. Symp. Circuits Syst. (ISCAS)*, Florence, Italy, 2018, pp. 1–4.
[12] Z. Cheng, X. Zheng, M. J. Deen, and H. Peng, "Recent developments and design challenges of high-performance ring oscillator CMOS time-to-digital converters," *IEEE Trans. Electron Devices*, vol. 63, no. 1, pp. 235–251, Jan. 2016.
[13] I. Vornicu, R. Carmona-Galán, and Á. Rodríguez-Vázquez "Arrayable voltage-controlled ring-oscillator for direct time-of-flight image sensors," *IEEE Trans. Circuits Syst. I, Reg. Papers*, vol. 64, no. 11, pp. 2821–2834, Nov. 2017.
[14] A. A. Abidi, "Phase noise and jitter in CMOS ring oscillators," *IEEE J. Solid-State Circuits*, vol. 41, no. 8, pp. 1803–1816, Aug. 2006.
[15] N. Da Dalt and A. Sheikholeslami, *Understanding Jitter and Phase Noise: A Circuits and Systems Perspective*. Cambridge, U.K.: Cambridge Univ. Press, 2018.
[16] A. Chorti and M. Brookes, "A spectral model for RF oscillators with power-law phase noise," *IEEE Trans. Circuits Syst. I, Reg. Papers*, vol. 53, no. 9, pp. 1989–1999, Sep. 2006.
[17] J. A. McNeill, "Jitter in ring oscillators," *IEEE J. Solid-State Circuits*, vol. 32, no. 6, pp. 870–879, Jun. 1997.
[18] S. Pavan, R. Schreier, and G. Temes, *Understanding Delta-Sigma Data Converters*, 2nd ed. Hoboken, NJ, USA: Wiley, 2017.
[19] S. Ziabakhsh, G. Gagnon, and G. W. Roberts, "The peak-SNR performances of voltage-mode versus time-mode circuits," *IEEE Trans. Circuits Syst. II, Exp. Briefs*, vol. 65, no. 12, pp. 1869–1873, Dec. 2018.